Snow Albedo Seasonal Decay and Its Relation With Shortwave Radiation, Surface Temperature and Topography Over an Antarctic Ice Cap

Javier F. Calleja, Rubén Muñiz, Susana Fernández, Alejandro Corbea-Pérez, Juanjo Peón, Jaime Otero, and Francisco Navarro

***Abstract*—We have characterized the snow albedo decay over Hurd Peninsula, Livingston Island, Antarctica, for the period 2000–2016. The snow albedo was obtained from the MOD10A1 product of the spaceborne MODIS sensor. A low-pass filter is applied to the data in order to eliminate short-term variations and retain the seasonal variation of albedo. The seasonal albedo was fitted to an exponential decay function to obtain the decay rate, the duration and the starting date of the decay. On average, albedo decay starts in late September and lasts for 96 $\pm$ 20 days. Snow melting lags behind snow albedo decay. This lag is due, on the one hand, to the occurrence of dry-snow metamorphism and sublimation in the early stages of the decay, and on the other hand to persisting subsurface melting after the completion of the metamorphic processes at the surface. The albedo decay is mainly driven by the shortwave incident radiation, with air and near-surface temperatures unexpectedly playing a minor role. Near-surface-temperature controls the importance of the local topography in the albedo decay. Topography only determines the albedo decay when the snow cover is not homogeneous over the study area.**

***Index Terms*—Antarctica, digital terrain model, remote sensing, shortwave radiation, snow albedo, snow metamorphism, temperature.**

I. Introduction

THE albedo of snow is very sensitive to the degree of metamorphism of the snow. The mechanisms controlling small-scale snowpack metamorphic processes that drive snow albedo decay are complicated and difficult to model accurately [1], [2]. What is experimentally observed, is that snow albedo changes over time including short-term variations (those that take place within hours to days), mid-term variations (changes through spring, summer, and autumn) [3], [4], [5], [6], [7], and long-term variations (changes accumulated over the years, giving rise to a long-term trend) [4], [6], [8]. It is well-known that in spring and summer, and despite occasional increases or decreases, snow albedo exhibits a decreasing trend associated to snow metamorphism and melting. Occasional snow albedo increases can be due to snowfall events or snow drift, while occasional snow albedo decreases can be due to erosion caused by strong winds [4]. A precise description of snow albedo decay is required because albedo is a key parameter in glacier surface mass balance models, which require precise values of albedo over glaciers [9], [10]. This highlights the need to characterize snow albedo decay distribution over glaciers and ice caps and to identify the driving mechanisms. Shortwave and longwave radiation, temperature, and topography are among them [11], [12]. Several models have been proposed to account for the change of albedo during spring and summer due to snow aging. For example, snow albedo has been proposed to decay over time according to an exponential [13], [14], [15] or a potential law [16]. Other authors have included factors like snow age, sun zenith angle, and snow surface temperature [17], [3], [18]. Snow albedo has also been modeled as a function of snow age, depth, density, and air temperature using multiple regression analysis [19]. Simple parameterizations have been used in surface and mass balance models just considering constant values of albedo for dry-snow, wet-snow an ice [20]. Whatever parameterization is used to describe the seasonal behavior of snow albedo, short-term variations must first be filtered out. In the case of remote sensing data series, this has been achieved applying a low-pass Butterworth filter to the data [21], [22].

In addition, snow albedo measured from satellite sensors may be affected by noise in the input data or errors in the algorithm. Another problem stems from the fact that satellite albedo can only be calculated in clear days, while a realistic description of albedo must include all-sky conditions. In a previous work [6], we showed that the daily snow albedo product of the Moderate Resolution Imaging Spectrometer (MODIS) sensor on board of the Terra platform (MOD10A1 product) tracks the seasonality

Manuscript received August 4, 2020; revised December 10, 2020; accepted January 4, 2021. Date of publication January 14, 2021; date of current version February 5, 2021. This work was supported in part by the Spanish Ministry of Science, Innovation and Universities under Grant CTM2014-52021-R and Grant CTM2017-84441-R. The work of Alejandro Corbea-Pérez was supported by the Ph.D. under Grant: "Severo Ochoa" from the Government of the Principality of Asturias [BP17-151]. *(Corresponding author: Javier Calleja.)*

Javier F. Calleja is with the Remote Sensing Applications Research Group, Department of Physics, University of Oviedo, 33007 Oviedo, Spain (e-mail: jfcalleja@uniovi.es).

Rubén Muñiz is with the Department of Computer Science, University of Oviedo, 33271 Gijón, Spain (e-mail: rubenms@uniovi.es).

Susana Fernández is with the Instituto de Ciencias y Tecnologías Espaciales de Asturias, Department of Geology, University of Oviedo, 33005 Oviedo, Spain (e-mail: fernandezmsusana@uniovi.es).

Alejandro Corbea-Pérez is with the Remote Sensing Applications Research Group, Department of Mining Exploitation and Prospecting, University of Oviedo, 33007 Oviedo, Spain (e-mail: corbeaalejandro@uniovi.es).

Juanjo Peón is with the Instituto de Ciencias y Tecnologías Espaciales de Asturias, University of Oviedo, 33005 Oviedo, Spain (e-mail: peonjuan@uniovi.es).

Jaime Otero and Francisco Navarro are with the Department of Applied Mathematics, Universidad Politécnica de Madrid, 28040 Madrid, Spain (e-mail: jaime.otero@upm.es; francisco.navarro@upm.es).

Digital Object Identifier 10.1109/JSTARS.2021.3051731

This work is licensed under a Creative Commons Attribution 4.0 License. For more information, see https://creativecommons.org/licenses/by/4.0/

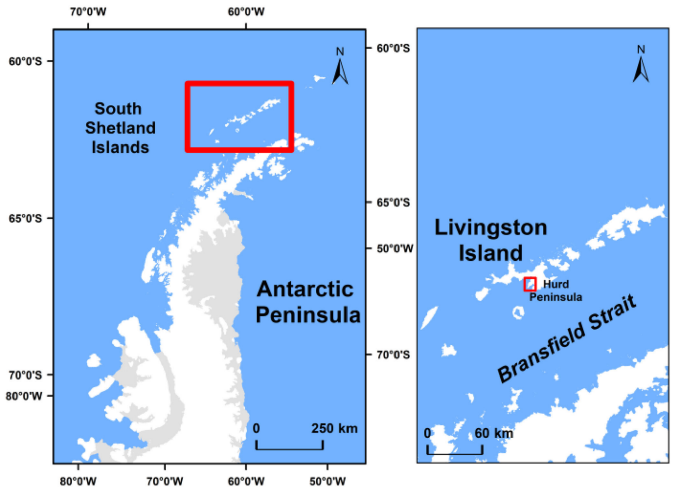

Fig. 1. Geographical setting of the study area.

and the trend of all-sky *in situ* data. This is achieved when MOD10A1 data are filtered using a maximum filter, which eliminates some extremely low and unrealistic values of albedo.

This article provides a precise description of the snow albedo decay distribution over an ice cap in Antarctica and identifies the mechanisms that drive this seasonal decay. The decay is described through the albedo decay rate, its duration and the onset date. We use the daily snow albedo product MOD10A1 (Version 6) [23]. In order to retain only the seasonal decay associated with snow metamorphism, short-term variations of albedo and MOD10A1 intrinsic noise are filtered out using a maximum filter combined with a low-pass Butterworth filter.

In Section II, we describe the study area. In Section III, we provide a detailed description of the data. We proceed with a thorough description of the data processing in Section IV. In Section V, we present the results, with the discussion in Section VI. Section VII concludes this article.

II. Geographical Setting

Hurd Peninsula is located on Livingston Island, Antarctica, covering an area of about 10 km^2 (see Figs. 1 and 2). It is permanently covered with ice along the year, except a few coastal locations in summer. The Spanish Meteorological Agency (Agencia Estatal de Meteorología, AEMET) operates two Automatic Weather Stations (AWS), one placed near Juan Carlos I station (JCI) and the other on Johnsons Glacier (JG). JCI AWS is located at 62° 39′ 48″S and 60° 23′ 19″ W at South Bay, 13 m above sea level [24]. JG AWS is inland, 178 m above sea level, and it was located at 62° 40′ 16″S and 60° 21′ 51″W until February 2015. The annual average temperature at JCI 1988 and 2014 was –1.2 °C, and the mean annual relative humidity was 83%. Precipitations were registered, on average, 162 days per year between 1988 and 2014, mainly in the form of snow, with some rain in summer.

The choice of Hurd Peninsula for this study is the availability of surface mass balance, equilibrium line altitude, and accumulation area ratio for its glaciers since 2002 [9], as these two glaciers have an ongoing monitoring programme whose data are supplied yearly to the World Glacier Monitoring Service database [25]. An additional advantage is the proximity of Hurd and Johnsons glaciers to the Spanish Antarctic Station Juan Carlos I.

III. Data

A. In Situ *Data*

In situ albedo, radiation and temperature were measured at the AWS at JCI Incident shortwave radiation energy S is measured at JCI using a pyranometer Kipp and Zonen CM11 in the range 300–2800 nm. A measurement is recorded every 10 min. The sum of all measurements recorded during one day provides the total S for that day. S corresponds to the total energy incident on a horizontal surface. The temperature at JCI is measured every 10 min at 2 m and 20 cm above the ground. The temperature recorded at 2 m is referred to as air temperature (T_a) throughout this article. The temperature at 20 cm is referred to as T_{20}. The ground at JCI is covered by snow and ice with a thickness above 50 cm from early July until mid-December [24], so T_{20} in spring corresponds to snow/ice temperature. *In situ* albedo is also obtained from two Kipp and Zonen CNR-1 pyranometers placed at JG, A measurement is acquired every 10 min. The spectral range is 300–2800 nm.

Mean daily values of S, T_a, and T_{20} for spring (September–November) are also calculated. To do so, mean daily and monthly values are calculated first. Daily, monthly and seasonal average values are only calculated if at least 80% of the data are recorded [26].

B. *Satellite Data*

Satellite snow albedo was obtained from the MODIS MOD10A1 (Collection 6) daily snow albedo product distributed by NASA's National Snow and Ice Data Center [23]. The daily MOD10A1 data are gridded using the MODIS Sinusoidal Tile Grid at 500 m spatial resolution. Snow albedo is calculated for the visible and near infrared bands using the MODIS land-surface reflectance product MOD09GA as input (bands 1 to 9 of MODIS sensor, covering the range 400–2100 nm). For the calculation of the snow albedo, the daily observation selected from multiple observations in a day in a grid cell is the observation acquired nearest nadir, nearest local noon and having the greatest coverage of the grid cell. An anisotropic response function is used to correct for anisotropic scattering effects, to calculate the narrowband albedo. A narrow-to-broadband conversion scheme is then used to create an integrated broadband albedo. MOD10A1 algorithm assumes that the incident radiation is in the form of a collimated beam, so it is direct-hemispherical reflectance (black-sky albedo). The daily snow albedo product MOD10A1provides: type of cover, snow albedo, and a basic quality assessment flag. The basic quality assessment (QA) is given the values 0 = best, 1 = good, 2 = OK, 3 = poor, and other (night, ocean, unusable data). For this work, we retained those pixels and dates classified as snow and with QA = 0 (best quality). Then, another filter was applied to keep only the pixels and dates for which the Sun Zenith Angle (SZA) is below 75° two hours before and after local noon. The last condition is met from September 1 until April 10 over Hurd Peninsula. Cloud and snow confusion in Collection 6 is similar to Collection 5

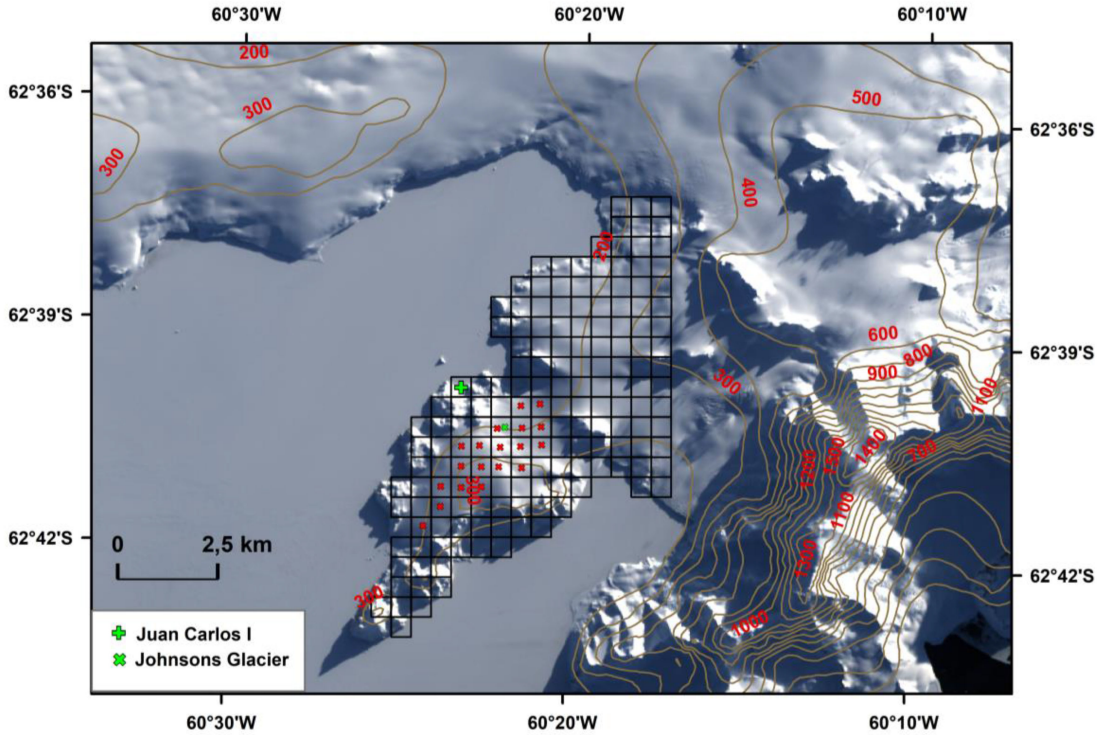

Fig. 2. Closer view of Hurd Peninsula and the location of the Automatic Weather Stations. The grid represents the MODIS pixels used in the study. Pixel marked with a red cross cover the surface of Hurd and Johnsons glaciers.

[23]. In a previous work [6], we evaluated the MOD10A1 cloud mask over Hurd Peninsula and showed that the performance was comparable to that over Greenland.

The MODIS/Terra surface reflectance product MOD09GA was used to mask the Hurd peninsula. We chose this product because it has the same spatial resolution as MOD10A1. When using MOD10A1, some water pixels are classified as snow. This may be due to the fact that the cloud mask does not work properly on that area or due to the existence of ice on the water surface. These pixels have to be eliminated. The product MOD09GA is distributed by NASA's Land Processes Distributed Active Archive Center. It provides an estimate of the surface spectral reflectance of MODIS bands 1 through 7, corrected for atmospheric conditions such as gasses, aerosols, and Rayleigh scattering in the sinusoidal projection, with a 500-m spatial resolution [27]. A MOD09GA image of January 16, 2014 was used. On that date the sky was clear over the study area and a mask was built using the condition that the reflectance of Band 1 was greater than 0.25. The resulting mask is the gridded area in Fig. 1. This mask was applied onto all the MOD10A1 images.

Both MOD10A1 and MOD09GA data were downloaded using the Google Earth Engine Application Programming Interface [28], [29]. All the images were reprojected to WGS84 UTM 20S projection.

C. Digital Terrain Model (DTM) and Topographic Variables

We used a 30-m DTM from the Reference Elevation Model of Antarctica (REMA) [30]. REMA is a high-resolution, time-stamped digital surface model (DSM) of Antarctica at 8-m spatial resolution. The DSM was downloaded from the Polar Geospatial Center, University of Minnesota [31]. The 8-m DSM was resampled to 30 m and all the topographic parameters were calculated using the 30 m DSM. Selection of the right DTM resolution is essential to capture the pattern of the relief related to the process under investigation. There are two types of relief at metric scales in the study area: the relief of bedrock areas with extremely rough surfaces and high steep slopes; and the relief on the glaciers, much smoother. The 30-m pixel represents the relief at decametric scales without any loss of information.

To obtain the DTM variables and topographic indexes, we used the system for automated geoscientific analyses (SAGA) that is an open-source geographic information system [32]. SAGA provides a set of tools ranging from the preprocessing of DTM (e.g., filtering and filling procedures) through the generation of simple first- and second-order terrain derivatives, such as slope and curvature, to more sophisticated terrain parameters, e.g., topographic position index (TPI) or wind exposition index (WEI) [33], [34]. Topographic shading controls surface insolation. Variations in elevation, slope, aspect, and local topographic horizon can cause substantial differences in solar radiation and thereby affect processes such as air and soil heating [35], [36]. Nevertheless, square grids of DTM cannot handle abrupt changes in elevation easily and they will often skip important details of the land surface in flat areas. For this reason, the use of topographic indices as the TPI or the WEI, can account for the component of the spatial variability of albedo that is due to topographic effects [33].

The TPI [37] is a dimensionless index that compares the elevation of each cell in a DEM to the mean elevation of a specified neighborhood around that cell. Positive TPI values represent locations that are higher than the average of their surroundings, as defined by the neighborhood (ridges). Negative TPI values represent locations that are lower than their surroundings (valleys). TPI values near zero are either flat areas (where the slope is near zero) or areas of constant slope (where the slope of the point is significantly greater than zero). Topographic position is an inherently scale-dependent phenomenon. The WEI [38] calculates the average wind effect for all directions using an angular step. Like the TPI, it is a dimensionless index. Values below 1 indicate wind shadowed areas, whereas values above 1 indicate areas exposed to wind.

For each MODIS pixel, we calculated the mean altitude, mean curvature, mean TPI, and mean WEI as the arithmetic mean of the 30-m pixel of the DTM contained in the MODIS pixel.

IV. Albedo Data Processing

A. *Processing of* In Situ *and MOD10A1 Albedo Data*

The filtering and processing of *in situ* albedo data was explained in detail in a previous work [6]. In order to avoid the great dependence of snow albedo on SZA [7], and the low reliability of measurements with SZA $> 75°$ [5], our analysis considered only data from 10 to 14 Local Solar Timer and from September 1 until April 10.

It has been demonstrated that MOD10A1 data track the seasonality and trend of all-sky *in situ* albedo data when filtered using a maximum filter [6], such that the snow albedo on date t_{n} is calculated using the data of three consecutive dates with MODIS data as follows:

$$\alpha\left(t_n\right) = \max\left(\alpha\left(t_{n-1}\right),\ \alpha\left(t_n\right),\ \alpha\left(t_{n+1}\right)\right). \tag{1}$$

The gap between two consecutive dates with MODIS data has a mean value of five days for all the pixels over the study area in the time span 2000–2016. In this article, we apply a maximum filter onto MOD10A1 followed by a second-order Butterworth filter with a normalized cutoff frequency of 0.1. The Butterworth filter filters short-term snow albedo variations, which facilitates the automated search of the start and end dates of the albedo decay as explained below. We used the implementation provided by Scipy, the well-known Python module. In a previous work [6], we estimated the onset and end dates of the albedo decay by visual inspection of the data.

B. *Snow Albedo Decay*

After processing the data as explained previously, we proceeded to characterize the snow albedo decay. We assume that snow albedo decays exponentially over time according to

$$\alpha\ (t) = \ \alpha_{\min} + A\exp\left(-\beta t\right) \tag{2}$$

where t is the number of days since the onset of the albedo decay, $\alpha_{\min}$ is the minimum albedo, A is a constant, and β is the albedo decay rate. The main problem is to establish the dates of the onset and end of the albedo decay. To do so, in the case of MODIS data, we used the albedo time derivative as follows. Once filtered, for each date, the time derivative of the albedo was calculated as

$$\left(\frac{d\alpha}{dt}\right)_{t_n} = \frac{\alpha\left(t_{n+1}\right) - \alpha\left(t_{n-1}\right)}{t_{n+1} - t_{n-1}}. \tag{3}$$

We assume that on date t_n the albedo is decaying if

$$\left(\frac{d\alpha}{dt}\right)_{t_n} < 0 \tag{4a}$$

or

$$\frac{1}{2}\left(\left(\frac{d\alpha}{dt}\right)_{t_{n+1}} + \left(\frac{d\alpha}{dt}\right)_{t_{n+2}}\right) < 0. \tag{4b}$$

Equations (4a) and (4b) mean that the albedo on date t_n is supposed to be decaying if either the derivative of the albedo at t_n is negative or the mean value of the derivative at the next two dates with albedo data is negative. The first condition is obvious; the second one was established to avoid stopping the decay when an albedo increase was followed by a continuing albedo decrease during the two following dates. The starting and end dates of the *in situ* albedo decay were computed using the procedure described previously. Because of the density of *in situ* data (nearly one datum per day) and the high frequency of *in situ* albedo variations this procedure could lead to stop the albedo decay on any of the local minima of the data series (like the one marked with a black arrow in season 2006–2007 in Fig. 3). In order to avoid this, we applied the procedure abovementioned using only the *in situ* data on dates with MODIS data.

Filtered albedo data were fitted to (2). Three parameters were obtained from the fit: $\alpha_{\min}$, A, and β along with their corresponding p-values. We also obtained the duration of the decay D and the date of the onset of the albedo decay for each season. The value $\alpha_{\min}$ is never attained because the duration of the decay is finite. The final value of the albedo at the end of the metamorphic processes will be

$$\alpha\ (D) = \ \alpha_{\min} + A\ \exp\left(-\beta D\right). \tag{5}$$

The total albedo decay depends on both β and D, and, according to (5)

$$ln\ \left(\frac{A}{\alpha\left(D\right) - \alpha_{\min}}\right) = \ \beta D. \tag{6}$$

If $\beta D\ \to \infty$, then $\alpha(D)\ \to \alpha_{\min}$ so βD is the key parameter that determines the degree of metamorphism attained at each location on the ice cap.

Regarding *in situ* data, the exponential fit was performed using all the *in situ* data available between the onset and the end of the albedo decay. We computed the *in situ* albedo decay only for seasons 2006–2007, 2007–2008, and 2008–2009 because these are the seasons for which the time spans with MODIS and *in situ* data overlap the most [6]. In the case of MODIS data, a fit was calculated for each pixel each season independently. Then, the mean value of each parameter over the study area was calculated each season considering only the pixels meeting all of the following conditions:

$$0 < \alpha_{\min} < 1 \tag{7a}$$

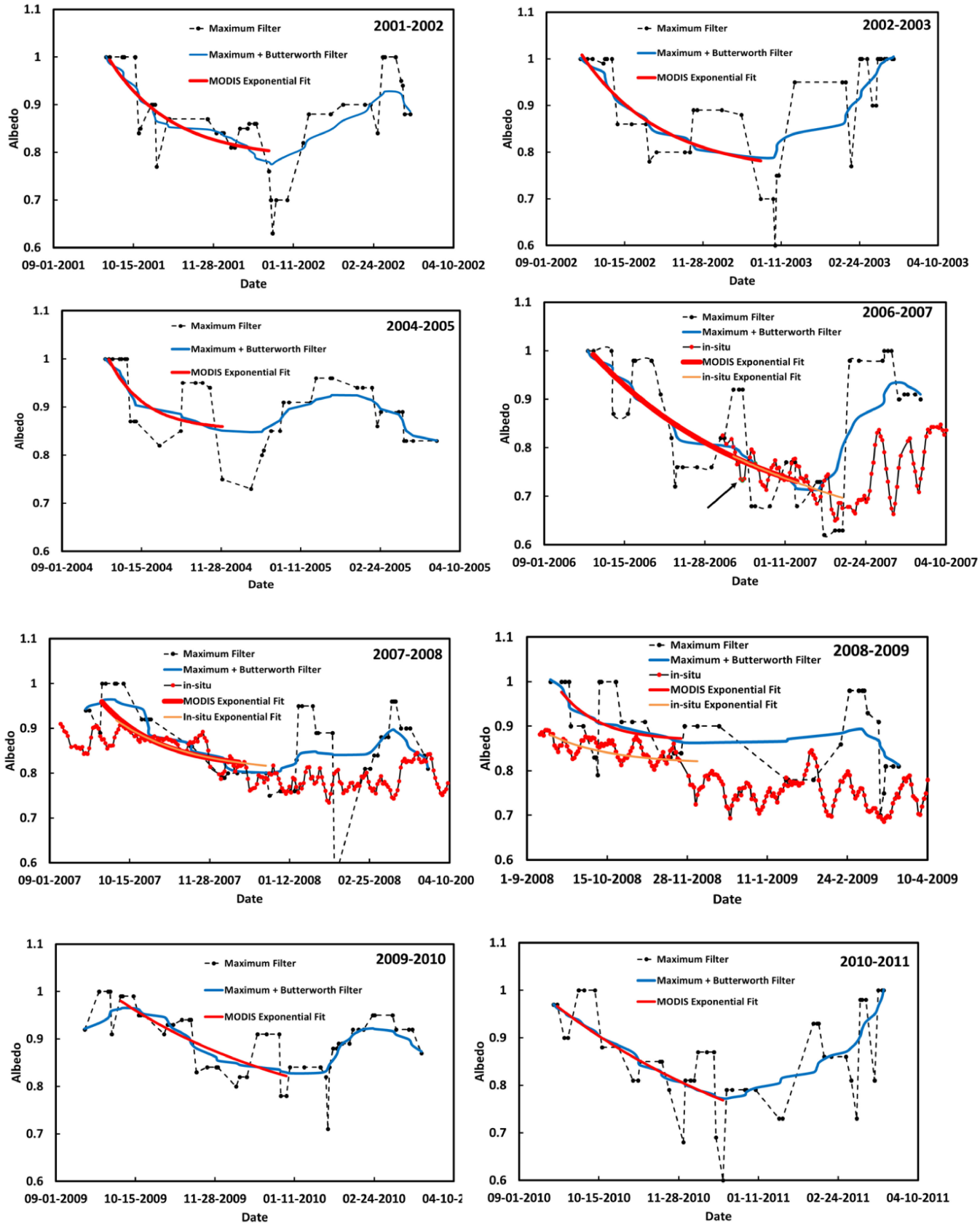

Fig. 3. Snow albedo from September 1 to April 10 from JG AWS and for the MODIS pixel containing the JG AWS. MOD10A1 daily snow albedo data filtered with a maximum filter and with a maximum filter followed by a Butterworth filter are displayed. The fit to an exponential is also shown. Only the seasons for which all the fit parameters were obtained with a statistical significance of $> 95\%$ are shown. The exponential fit is displayed between the calculated dates for the onset and end of the albedo decay. The black arrow indicates the position of a local minimum in the *in situ* data.

TABLE I
RMSD BETWEEN *IN SITU* ALBEDO AND MOD10A1 ALBEDO WITH DIFFERENT FILTERS

Season	MOD10A1 original	MOD10A1 maximum	MOD10A1 max + Butt
2006-07	0.15	0.16	0.10
2007-08	0.15	0.10	0.07
2008-09	0.12	0.12	0.11
2009-10	0.13	0.12	0.10
2010-11	0.16	0.17	0.11
2011-12	0.12	0.15	0.09
2012-13	0.26	0.24	0.18
2013-14	0.13	0.14	0.16
2014-15	0.15	0.08	0.06
Average	0.15	0.14	0.10

$$0 < A < 1 \tag{7b}$$

$$\beta > 0 \tag{7c}$$

$$p - \text{value } (\alpha_{\min}) < 0.05 \tag{7d}$$

$$p - \text{value } (A) < 0.05 \tag{7e}$$

$$p - \text{value } (\beta) < 0.05. \tag{7f}$$

V. RESULTS

A. MOD10A1 Filtering

The effect of the Butterworth filter with a normalized cutoff frequency of 0.1 on the MOD10A1 data is shown in Fig. 3. As an example, we show MOD10A1 data filtered with the maximum filter and with the maximum and Butterworth filter combined for the pixel on which the AWS at Johnsons Glacier is located. The low-pass Butterworth filter has been used in the frame of remote sensing time series as a means to reduce high-frequency noise or signals [21], [22]. It is clear from Fig. 3 that, even after the application of the maximum filter, some peaks in the signal remain. These short-term variations are smoothed with the application of the Butterworth filter. We have calculated the root-mean-square difference (RMSD) between the five-day window averaged *in situ* data and MOD10A1 data (see Table I). RMSD is calculated as

$$\text{RMSD} = \sqrt{\frac{\sum_{i=1}^{n} \left(\alpha_{\text{MOD10A1},\, i} - \alpha_{in\ situ,\, i}\right)^2}{n}} \tag{8}$$

with $\alpha_{\text{MOD10A1,i}}$ the albedo from MOD10A1 (the original data, the data filtered with a maximum filter or the data filtered with a maximum filter followed by a Butterworth filter with a normalized cutoff frequency of 0.1), and $\alpha_{in\ situ,\text{i}}$ the five-window moving averaged *in situ* albedo. The number of dates with both *in situ* and satellite data in (8) is n. The best results were obtained filtering MOD10A1 data with a maximum filter followed by a Butterworth filter with a normalized cutoff frequency of 0.1.

B. Snow Albedo Decay

The comparison between *in situ* and MODIS albedo decay parameters is shown in Table II. *In situ* albedo data are from the JG AWS and MODIS data correspond to the pixel on which JG AWS is located.

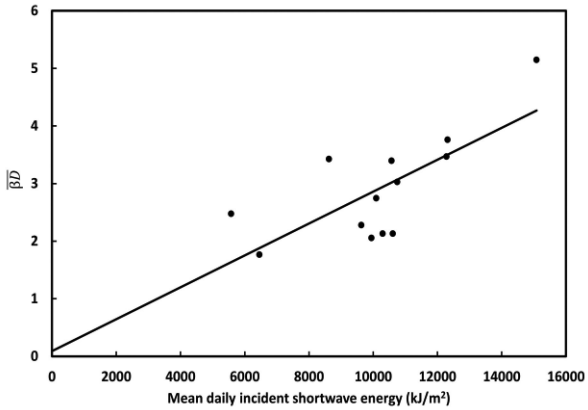

Fig. 4. Mean value of the albedo decay rate times the decay duration over Hurd Peninsula against the mean daily incident shortwave radiation from the AWS at Juan Carlos I Station in the period 2000–2015.

The mean values of $\alpha_{\min}$, A, β, D, and βD over the Hurd Peninsula for each season are given in Table III. The number of pixels meeting conditions (7a–7f) each season is N in Table III. The values in each row in Table III are the spatial averages over the study area for each season. We also calculated the total average over the study area and from 2000 to 2016 of D and of the onset in the last row of Table III.

The question arises of the dependence of the mean values obtained in Table III on the pixels available for the calculation. We computed the mean values of the albedo decay parameters for the pixels covering Hurd and Johnsons glaciers, an area permanently covered by snow or ice, and over which mass balance measurements have been carried out [9]. These pixels are marked with a red cross in Fig. 2. For the comparison with the whole study area, we show in Table IV, the results for the seasons for which the number of pixels marked with a red cross was at least ten.

C. Snow Albedo Decay Against Temperature and Radiation

The daily mean values of the shortwave energy per unit area, air temperature, and the temperature 20 cm above the ground are shown in Table V. We consider the spring values from the AWS because most of the albedo decay takes place in that period. We assume that radiation and temperature data from JCI are representative of the whole Hurd Peninsula, as demonstrated in previous works [9]. We investigated the relationship between the mean values of $\alpha_{\min}$, A, β, D, and $\beta\, D$ over Hurd Peninsula and the spring mean values of T_a, T_{20}, and S. The coefficients of linear correlation between the albedo decay parameters and S, T_{a}, and T_{20} are given in Table VI. The relation between $\overline{\beta D}$ and S is displayed in Fig. 4.

D. Snow Albedo Decay and Topography

The dependence of $\alpha_{\min}$, A, β, D, and βD on topography was also studied. The topographic variables mean Altitude,

TABLE II
COMPARISON OF *IN SITU* AND MODIS ALBEDO DECAY PARAMETERS

Season	α_{min}	A	β(day^{-1})	D (days)	βD	Onset (mm/dd)
2006-07	0.53 / 0.62	0.43 / 0.37	0.007 / 0.011	− / 111	− / 1.22	− / 9/28
2007-08	0.80 / 0.81	0.12 / 0.15	0.024 / 0.030	83 / 74	1.99 / 2.22	10/8 / 9/30
2008-09	0.82 / 0.87	0.07 / 0.11	0.030 / 0.046	81 / 66	2.43 / 3.04	9/14 / 9/20

Albedo decay parameters of *in-situ* data from JG AWS and of the MODIS pixel on which JG AWS is located. Values are given in the order *in-situ* / MODIS. Duration (D) and Onset are not given for 2006–07 season for *in-situ* albedo because of the lack of data at the beginning of the season.

TABLE III
ALBEDO DECAY DATA AVERAGED OVER HURD PENINSULA

Season	$\overline{\alpha_{min}}$	$\overline{A}$	$\overline{\beta}$ (day^{-1})	$\overline{D}$(days)	$\overline{\beta D}$	N	Onset (mm/dd) (σ(days))
2000-01	0.70 (0.09)	0.21 (0.10)	0.038 (0.029)	94 (43)	3.42 (2.80)	69	9/24 (8)
2001-02	0.79 (0.05)	0.14 (0.05)	0.036 (0.019)	84 (26)	2.95 (1.71)	45	10/7 (6)
2002-03	0.70 (0.07)	0.24 (0.08)	0.023 (0.020)	86 (27)	1.77 (0.94)	84	9/25 (5)
2003-04	0.75 (0.07)	0.17 (0.08)	0.031 (0.021)	124 (41)	3.47 (2.13)	50	10/5 (11)
2004-05	0.82 (0.04)	0.11 (0.04)	0.054 (0.042)	64 (42)	5.15 (3.54)	61	9/28 (5)
2005-06	0.77 (0.07)	0.17 (0.08)	0.031 (0.015)	71(22)	2.11 (1.04)	38	9/28 (8)
2006-07	0.63 (0.11)	0.31 (0.11)	0.016 (0.010)	131 (24)	2.13 (1.63)	86	9/28 (6)
2007-08	0.72 (0.08)	0.22 (0.09)	0.031 (0.027)	114 (45)	3.40 (2.35)	99	9/29 (5)
2008-09	0.78 (0.07)	0.13 (0.08)	0.028 (0.020)	99 (48)	2.47 (1.68)	26	9/30 (11)
2009-10	0.75 (0.07)	0.15 (0.07)	0.036 (0.028)	110 (36)	3.76 (2.54)	82	9/29 (13)
2010-11	0.69 (0.08)	0.20 (0.09)	0.027 (0.028)	92 (22)	2.28 (1.88)	55	9/26 (5)
2011-12	0.68 (0.06)	0.28 (0.09)	0.027 (0.017)	82(32)	2.13 (1.55)	80	9/22 (3)
2012-13	0.78 (0.10)	0.13 (0.08)	0.038 (0.037)	95 (47)	2.74 (1.78)	35	9/23 (4)
2013-14	0.72 (0.08)	0.17 (0.10)	0.029 (0.032)	126 (35)	3.03 (1.83)	16	10/3 (9)
2014-15	0.73 (0.06)	0.21 (0.07)	0.027 (0.020)	78 (22)	2.05 (1.50)	31	9/25 (6)
2015-16	0.69 (0.10)	0.22 (0.10)	0.024 (0.026)	80 (20)	1.66 (0.75)	54	10/1 (4)
Average				96 (20)			9/28 (4)

Mean values over Hurd Peninsula of the albedo decay parameters $\alpha_{\min}$, A, β, albedo decay duration D, βD, and the mean date for the onset of the decay. N is the number of pixels used to calculate the mean values for each season. The standard deviation is given in parenthesis. The time averages from 2000 to 2016 are calculated for D and the onset in the last row.

TABLE IV
ALBEDO DECAY DATA AVERAGED OVER HURD AND JOHNSONS GLACIERS

Season	$\overline{\alpha_{min}}$	$\overline{A}$	$\overline{\beta}$ (day^{-1})	$\overline{D}$ (days)	$\overline{\beta D}$	N	Onset (mm/dd) (σ(days))
2001-02	0.77 (0.02)	0.17 (0.06)	0.044 (0.024)	75 (17)	3.01 (1.63)	11	10/5 (4)
2002-03	0.71 (0.05)	0.21 (0.07)	0.024 (0.012)	67 (21)	1.63 (1.31)	14	9/27 (5)
2003-04	0.75 (0.04)	0.11 (0.06)	0.036 (0.025)	121 (41)	4.23 (3.44)	10	10/18 (11)
2007-08	0.71 (0.10)	0.24 (0.12)	0.035 (0.023)	112 (45)	3.56 (2.13)	15	9/30 (7)
2009-10	0.71 (0.08)	0.19 (0.10)	0.028 (0.019)	107 (31)	2.90 (2.33)	10	9/24 (5)
2010-11	0.64 (0.10)	0.29 (0.13)	0.029 (0.028)	83 (9)	2.27 (2.12)	10	9/25 (5)
Average				94 (22)			10/1 (9)

Mean values over Hurd and Johnsons glaciers of the albedo decay parameters $\alpha_{\min}$, A, β, albedo decay duration D, βD, and the mean date for the onset of the decay. N is the number of pixels used to calculate the mean values for each season. The standard deviation is given in parenthesis. Only seasons with N at least 10 are shown.

mean Curvature, mean TPI, mean WEI, were selected because they provided the best results. The range of variation of these variables is summarized in Table VII. Maximum, minimum, mean, median, and standard deviation values were calculated taking into account the pixels considered in the calculation of the parameters in Table III. We calculated the coefficient of linear correlation between the decay parameters and topographic variables $r_{\text{decay-topo}}$, where the subscript "decay" stands for $\alpha_{\min}$, A, β, D, and βD and the subscript "topo" stands for mean altitude, mean curvature, mean TPI, and mean WEI. The coefficients of linear correlation $r_{\text{decay-topo}}$ are low, but it is worth noting the close relation between $r_{\text{decay-topo}}$ and the spring near-surface temperature T_{20}. In Fig. 5, we show the evolution of $r_{\text{decay-topo}}$ and of T_{20} in the period 2000–2014. They follow exactly the same pattern. In order to study the role of temperature in the dependence of $\alpha_{\min}$, A, β, D, and βD on topography, we obtained the linear coefficient of correlation of $r_{\text{decay-topo}}$ and T_{20}. It is evident that the correlation between albedo decay and topography is determined by T_{20}. This will be discussed in detail below. Table VIII shows the coefficient of

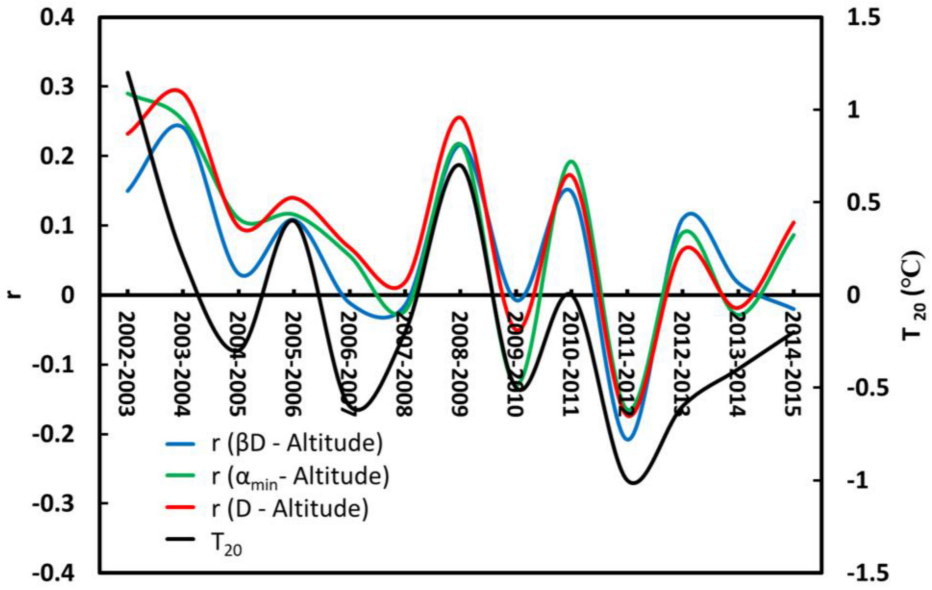

Fig. 5. Coefficient of correlation between Altitude and βD, $\alpha_{\min}$, and D over Hurd Peninsula over the period 2002–2015. Spring (September–November) temperature at 20 cm above ground measured at the AWS in Juan Carlos I Station in the period 2001–2016.

TABLE V
DAILY MEAN VALUES OF SHORTWAVE INCIDENT ENERGY, TEMPERATURE AT 20 CM AND AIR TEMPERATURE AT JUAN CARLOS I STATION FOR SPRING (SEPTEMBER-OCTOBER-NOVEMBER)

Season	S (kJ/m^2)	T_{20} (°C)	T_a (°C)
2000-01	8623	-	−6.7
2001-02	-	-	-
2002-03	6457	1.2	−4.6
2003-04	12286	-	−0.4
2004-05	15085	−0.3	1.1
2005-06	-	0.4	−2.4
2006-07	10612	−0.6	−1.0
2007-08	10571	−0.2	−1.6
2008-09	5578	0.7	−0.1
2009-10	12315	−0.5	−2.7
2010-11	9633	0.0	−0.7
2011-12	10294	−1.0	−2.2
2012-13	10099	−0.6	−2.8
2013-14	10749	−0.4	−2.7
2014-15	9946	−0.2	−2.3
2015-16	-	-	-

TABLE VI
COEFFICIENT OF CORRELATION OF SNOW ALBEDO DECAY PARAMETERS WITH SPRING SHORTWAVE RADIATION AND TEMPERATURE

	$\overline{\alpha_{min}}$	$\bar{A}$	$\bar{\beta}$	$\overline{\beta D}$
S	0.29	−0.23	0.62	0.72
T_{20}	0.17	−0.18	−0.13	−0.30
T_a	0.10	−0.07	−0.39	−0.11

correlation between $r_{\text{decay-topo}}$ and T_{20}. All the values given are statistically significant at a 95% level.

TABLE VII
TOPOGRAPHIC VARIABLES OVER HURD PENINSULA

	Altitude (m)	Curvature	TPI	WEI
Max	321.6	0.007	1.023	1.17
Min	0.5	-0.007	-0.796	0.86
Mean	155.8	2×10^{-6}	0.004	1.01
Median	156.5	-4×10^{-5}	-0.005	1.01
σ	75.8	0.002	0.200	0.06

TABLE VIII
COEFFICIENT OF CORRELATION BETWEEN $R_{\text{DECAY-TOPO}}$ AND T_{20}

	Altitude	Curvature	TPI	WEI
$\alpha_{\min}$	0.83	0.82	0.80	0.65
A	0.79	0.77	0.78	0.48
β	0.55	0.74	0.67	0.69
D	0.85	0.84	0.83	0.64
βD	0.77	0.73	0.71	0.84

VI. DISCUSSION

In this section, we discuss first the role of the low-pass Butterworth filter. We then discuss the relation of albedo decay with radiation, topography, and temperature.

Although snow albedo can suffer abrupt changes due to occasional snowfall events, snow drift or to refreezing events in cold periods or during the night, these can be filtered out and the mid-term (along the season) albedo variation can be described using the exponential law given by (2). Moreover, our results show that the use of the maximum filter onto MOD10A1 snow albedo to eliminate unrealistic extremely low albedo values, followed by the Butterworth filter to eliminate short-term albedo fluctuations, is an appropriate procedure to describe the seasonal albedo decay. The RMSD between satellite and *in situ* albedo

data is diminished when using the Butterworth filter (see Table I). The comparison of the albedo decay from *in situ* and MODIS data (see Fig. 3 and Table II) demonstrats that filtered MOD10A1 daily albedo captures the variability of the albedo: the decay parameters (including the onset and the duration) from both datasets agree reasonably well. It is remarkable that the snow albedo decay is linked to an ongoing snow metamorphism, which occurs along spring, although interrupted from time to time by occasional events. In this regard, it has been observed that daily variations of the specific surface area (SSA) of snow at Dome C, Antarctica, that occur in the top millimeters are superimposed to a seasonal decrease of the SSA from October to February [4]. This mechanism is expected to occur in Hurd Peninsula as well.

The study area is too small compared to the pixel size of MODIS to screen areas of interest. Moreover, the number of pixels available to compute averages over small regions of interest may be reduced due to the high cloudiness of the area; this is why we selected a study area larger than that covered by Hurd and Johnsons glaciers. According to Tables III and IV, the seasonal mean values computed over the whole study area agree with those calculated over Hurd and Johnsons glaciers. This demonstrates that the influence of snow-free areas in the values computed in Table III is negligible. The results in Table III can be considered representative of the phenomena occurring over Hurd and Johnsons glaciers. The discussion that follows is based on Table III. The snow albedo decay starts soon in spring. The mean date for the onset of the snow albedo decay in the period 2000–2016 is September 28, and the mean albedo decay duration is 96 $\pm$ 20 days. We conclude that most of the snow albedo decay takes place in the period from late September to December. Previous investigations of mass balance over the Hurd Peninsula have established that the snow melt in Hurd Peninsula takes place mostly from December to March [10], [9]. The fact that snow melting lags behind albedo decay can be explained, if we consider that some surface snow metamorphic processes occur prior to melting and that melting continues after surface snow has attained its maximum degree of metamorphism. Snow metamorphism starts immediately after snow falls onto the surface. Metamorphism in dry snow takes place before melting via vapor diffusion over ice crystal surfaces and sublimation of vapor into the atmosphere. Vapor diffusion can occur in the absence of temperature gradients, producing rounded ice grains, and it can be accelerated by temperature gradients, producing faceted grains [2], [1]. The persistence of snow melting even after surface snow albedo decay is completed can be explained by subsurface melting [39].

The correlation between $\overline{\beta D}$ and S is strong (see Table VI and Fig. 4). Snow albedo decays occurs due to snow metamorphism. Starting at $\alpha(0)$ in September, α should reduce its value down to the theoretical value $\alpha_{\min}$, a value that is not attained because snow metamorphism gets to its final point at a finite time D. Snow reaches a degree of metamorphism that is described by the quantity βD. The albedo decay is mostly driven by the absorption of shortwave radiation, while air and near- surface temperature do not play a major role. Recent theoretical calculations have shown that the heating of snow and ice in polar areas is mainly caused by the absorption of shortwave radiation [40], producing temperature gradients near the surface that accelerate snow metamorphism, and, as a consequence, the snow albedo decay. It is remarkable the influence of the incident shortwave radiation on the albedo decay regardless of the topography (S is measured on a horizontal surface). This is due to the high cloudiness of the area [26], [10], because topographic effects are much less important for diffuse radiation than for direct radiation [11]. It is obvious from Table VI that, while S alone explains a great part of the albedo decay over the area, $T_{\rm a}$ and T_{20} separately do not. The role of topography seems to be more complicated. The coefficients of correlation between the topographic variables and $\alpha_{\min}$, A, β, D, and βD are indeed very low but vary in magnitude and over the years following the same pattern as T_{20} (see Fig. 5). The coefficients of correlation of $r_{\text{decay-topo}}$ with T_{20} are all positive and very high. The results in Table VIII show that the effect of topography in the snow albedo decay is important when the spring near-surface temperature is high. However, when the spring near-surface temperature in the area is low, the snow albedo decay seems to depend poorly on the topography of the site. Let us note that from around July until December the ground is covered by a sufficiently thick snow layer and, thus, T_{20} represents the temperature of the snow. Thus, a high value of T_{20} in spring means that the snow cover at JCI is already close to melting in spring. In these circumstances, we expect the snow cover in Hurd Peninsula along spring to be more inhomogeneous, with patches of snow in an advanced metamorphic state, shallow snow and even bare soil or ice. On the other hand, low values of T_{20} mean that the extension of snow cover is larger in spring and probably in a more homogeneous metamorphic state over the whole Hurd Peninsula.

The role of temperature, radiation, and snowpack aging on snow albedo has been studied by several authors. In another work, snow age and air temperature at 2 m above ground have been found to be the most important determinants of surface snow albedo for both shallow and deep snow covers [19]. It is remarkable that in that work neither radiation nor topography were considered; and in our case air temperature does not seem to be a determinant physical quantity. Recent studies of snow metamorphism at Dome C have concluded that in the top 10 cm the increase in specific surface area is due to an increase of air temperature and solar radiation [4]. From our results, we conclude that the role of temperature is determinant only on flat areas with a homogeneous snow cover.

VII. Conclusion

We have shown that the seasonal albedo decay on an Antarctic ice cap can be fully described using the daily snow albedo product MOD10A1 (version 6) filtered with a maximum filter followed by a second-order Butterworth filter with a normalized cutoff frequency of 0.1. The filtering allows for the short-term albedo variations to be filtered, keeping only albedo variations associated with seasonal snow metamorphism. The snow albedo decay over time is well described by an exponential function. On average, snow albedo decay starts in late September and lasts for around 96 days. Snow melting lags behind albedo decay, due to dry metamorphism in the initial metamorphic stages and

to persisting subsurface snow melting once the metamorphic processes of snow at the surface have been completed. Snow albedo decay is mainly driven by the absorption of shortwave radiation in spring. Surprisingly, surface and air temperature play a minor role. The topography of the ice cap is determinant only when the snow cover is not homogeneous. Further research is underway to extend the present procedure to larger areas in Antarctica. The role of other topographic and weather variables is also under investigation.

REFERENCES

[1] D. R. DeWalle and A. Rango, "Snowpack condition," in *Principles of Snow Hydrology*, 1st ed., D. R. DeWalle, A. Rango, and E. Cambridgge, Eds. Cambridge, U.K.: Cambridge Univ. Press, 2008, pp. 48–75.

[2] K. M. Cuffey and W. S. B. Paterson, "Grain-scale structures and deformation of ice," in *The Physics of Glaciers*, 4th ed., B. Heinemann, Ed. Oxford, U.K.: Elsevier, 2010, pp. 29–89.

[3] M. J. Malik, R. van der Velde, Z. Vekerdy, and Z. Su, "Improving modeled snow albedo estimates during the spring melt season," *J. Geophys. Res. Atmos.*, vol. 119, no. 12, pp. 7311–7331, 2014.

[4] Q. Libois *et al.*, "Summertime evolution of snow specific surface area close to the surface on the Antarctic plateau," *Cryosphere*, vol. 9, no. 6, pp. 2383–2398, 2015.

[5] X. Wang and C. S. Zender, "Arctic and antarctic diurnal and seasonal variations of snow albedo from multiyear baseline surface radiation network measurements," *J. Geophys. Res. Earth Surf.*, vol. 116, no. F3, 2011, Art. no. F03008.

[6] J. F. Calleja, A. Corbea-Pérez, S. Fernández, C. Recondo, J. Peón, and M. Á. de Pablo, "Snow albedo seasonality and trend from MODIS sensor and ground data at Johnsons glacier, Livingston Island, Maritime Antarctica," *Sensors*, vol. 19, no. 16, 2019, Art. no. 3569.

[7] R. Pirazzini, "Surface albedo measurements over antarctic sites in summer," *J. Geophys. Res. Atmos.*, vol. 109, no. D20, 2004, Art. no. D20118.

[8] C. S. L. Minji Seo, H.-C. Kim, M. Huh, J.-M. Yeom, K.-S. H. Kyeong-Sang Lee, and S. Choi, "Long-term variability of surface albedo and its correlation with climatic variables over antarctica," *Remote Sens*, vol. 8, 2016, Art. no. 981.

[9] F. J. Navarro, U. Y. Jonsell, M. I. Corcuera, and A. Martín-Español, "Decelerated mass loss of hurd and Johnsons glaciers, Livingston Island, Antarctic Peninsula," *J. Glaciology*, vol. 59, no. 213, pp. 115–128, 2013.

[10] U. Y. Jonsell, F. J. Navarro, M. Bañón, J. J. Lapazaran, and J. Otero, "Sensitivity of a distributed temperature-radiation index melt model based on AWS observations and surface energy balance fluxes, hurd Peninsula glaciers, Livingston Island, Antarctica," *Cryosphere*, vol. 6, no. 3, pp. 539–552, 2012.

[11] D. R. DeWalle and A. Rango, "Snowpack energy exchange: Topographic and forest effects," in *Principles of Snow Hydrology*, 1st ed., D. R. DeWalle and A. Rango, Eds. Cambridge, U.K.: Cambridge Univ. Press, 2008, pp. 182–210.

[12] K. M. Cuffey and W. S. B. Paterson, "Mass balance processes: 2. Surface ablation and energy budget," in *The Physics of Glaciers*, 4th ed., B.-Heinemann, Ed. Oxford, U.K.: Elsevier, 2010, pp. 137–173.

[13] D. L. Verseghy, "Class—A Canadian land surface scheme for GCMS. I. Soil model," *Int. J. Climatol.*, vol. 11, no. 2, pp. 111–133, 1991.

[14] J. Oerlemans and W. H. Knapp, "A 1 year record of global radiation and albedo in the ablation zone of Morteratschgletscher, Switzerland," *J. Glaciology*, vol. 44, no. 147, pp. 231–238, 1998.

[15] M. Bougamont, J. L. Bamber, and W. Greuell, "A surface mass balance model for the Greenland ice sheet," *J. Geophys. Res. Earth Surf.*, vol. 110, no. F4, 2005, Art. no. F04018.

[16] B. Livneh, Y. Xia, K. E. Mitchell, M. B. Ek, and D. P. Lettenmaier, "Noah LSM snow model diagnostics and enhancements," *J. Hydrometeorol.*, vol. 11, no. 3, pp. 721–738, 2010.

[17] R. E. Dickinson, A. Henderson-Sellers, and P. J. Kennedy, "Biospher-Atmosphere transfer scheme (BATS) version 1e as coupled to the NCAR community climate model," Boulder, CO, USA, Aug. 1993, pp. 1–72.

[18] T. Aoki, A. Hachikubo, and M. Hori, "Effects of snow physical parameters on shortwave broadband albedos," *J. Geophys. Res. Atmos.*, vol. 108, no. D19, 2003, Art. no. 4616.

[19] T. Amaral, C. P. Wake, J. E. Dibb, E. A. Burakowski, and M. Stampone, "A simple model of snow albedo decay using observations from the community collaborative rain, hail, and snow-albedo (CoCoRaHS-Albedo) network," *J. Glaciology*, vol. 63, no. 241, pp. 877–887, 2017.

[20] T. Zolles and A. Born, "Sensitivity of the Greenland mass and energy balance to uncertainties in key model parameters," *Cryosphere Discuss.*, vol. 2019, pp. 1–25, 2019.

[21] J. Roberts and T. D. Roberts, "Use of the Butterworth low-pass filter for oceanographic data," *J. Geophys. Res. Ocean.*, vol. 83, no. C11, pp. 5510–5514, 1978.

[22] B. R. Scanlon, L. Longuevergne, and D. Long, "Ground referencing GRACE satellite estimates of groundwater storage changes in the California central valley, USA," *Water Resour. Res.*, vol. 48, no. 4, 2012, Art. no. W04520.

[23] D. K. Hall, V. V. Salomonson, and G. A. Riggs, "MODIS/Terra snow cover daily L3 global 500m grid. Version 6," *NASA Nat. Snow Ice Data Center Distrib. Act. Arch. Center*, 2016. Accessed: Jul. 1, 2020. [Online]. Available: https://nsidc.org/data/MOD10A1/versions/6

[24] M. Bañón, A. Justel, D. Velázquez, and A. Quesada, "Regional weather survey on Byers Peninsula, Livingston Island, South Shetland Islands, Antarctica," *Antarctic Sci.*, vol. 25, no. 2, pp. 146–156, 2013.

[25] "World glacier monitoring service." Accessed: Aug. 12, 2020. [Online]. Available: https://wgms.ch/

[26] M. Bañón and F. Vasallo, "The Spanish meteorological agency in Antarctica." (in Spanish), 2015, pp. 1–152.

[27] E. Vermote and R. Wolfe, "MOD09GA MODIS/Terra surface reflectance daily L2G global 1km and 500 m SIN grid V006," *NASA EOSDIS Land Processes DAAC*, 2015. Accessed: Jul. 1, 2020. [Online]. Available: https://doi.org/10.5067/MODIS/MOD09GA.006

[28] N. Gorelick, M. Hancher, M. Dixon, S. Ilyushchenko, D. Thau, and R. Moore, "Google Earth Engine: Planetary-scale geospatial analysis for everyone," *Remote Sens. Environ.*, vol. 202, pp. 18–27, 2017.

[29] "Google Earth Engine API." Accessed: Jul. 1, 2020. [Online]. Available: https://code.earthengine.google.com/

[30] I. M. Howat, C. Porter, B. E. Smith, M.-J. Noh, and P. Morin, "The reference elevation model of Antarctica," *Cryosphere*, vol. 13, no. 2, pp. 665–674, 2019.

[31] U. of Minnesota, "Polar elevation resources." Accessed: Jul. 1, 2020. [Online]. Available: https://www.pgc.umn.edu/guides/misc/polar-elevation-resources/

[32] O. Conrad *et al.*, "System for automated geoscientific analyses (SAGA) v. 2.1.4," *Geosci. Model Dev.*, vol. 8, no. 7, pp. 1991–2007, 2015.

[33] J. P. Wilson and J. C. Gallant, "Digital terrain analysis," in *Terrain Analysis: Principles and Applications, First*, J. P. Wilson and J. C. Gallant, Eds. New York, NY, USA: Wiley,, 2000, pp. 1–21.

[34] V. Olaya and O. Conrad, "Chapter 12 geomorphometry in SAGA," *Geomorphometry*, vol. 33, pp. 293–308, 2009.

[35] C. R. Duguay and E. F. Ledrew, "Estimating surface reflectance and albedo from Landsat-5 thematic mapper over rugged terrain," *Photogrammetric Eng. Remote Sens.*, vol. 58, no. 5, pp. 551–558, May 1992.

[36] R. Dubayah and P. M. Rich, "Topographic solar radiation models for GIS," *Int. J. Geogr. Inf. Syst.*, vol. 9, no. 4, pp. 405–419, Jul. 1995.

[37] A. Guisan, S. B. Weiss, and A. D. Weiss, "GLM versus CCA spatial modeling of plant species distribution," *Plant Ecology*, vol. 143, no. 1, pp. 107–122, 1999.

[38] J. Böhner and O. Antonić, "Chapter 8 land-surface parameters specific to topo-climatology," *Geomorphometry*, vol. 33, pp. 195–226, 2009.

[39] G. Koh and R. Jordan, "Sub-surface melting in a seasonal snow cover," *J. Glaciol.*, vol. 41, no. 139, pp. 474–482, 1995.

[40] L. A. Dombrovsky, A. A. Kokhanovsky, and J. H. Randrianalisoa, "On snowpack heating by solar radiation: A computational model," *J. Quantitative Spectrosc. Radiat. Transf.*, vol. 227, pp. 72–85, 2019.

Javier F. Calleja was born in Gijón, Spain, in 1966. He received the B.S. degree from the University of Zaragoza, Zaragoza, Spain, in 1989 and the Ph.D. degree from the University of Oviedo, Asturias, Spain, in 1997, both in physics.

He was with the University of Zaragoza, with the University of Oviedo, and as Research Fellow with the Centre for Data Storage Materials, Coventry University, U.K. He is currently an Associate Professor with the Department of Physics, University of Oviedo, Oviedo, Spain. His research interests include optical remote sensing, and snow and ice dynamics over ice caps.

Rubén Muñiz was born in Gijón, Spain, in 1973. He received the M.S. and Ph.D. degrees in computer science from the University of Oviedo, Asturias, Spain, in 1997 and 2003, respectively.

He is currently a Senior Lecturer with the Department of Computer Science, University of Oviedo, Asturias, Spain. His research interests include computer vision, pattern recognition, deep learning, home automation technologies, and IoT.

Susana Fernández received the M.S. degree in geological sciences and the Ph.D. degree in geomorphology sciences from the University of Oviedo, Asturias, Spain, in 1991 and 2005, respectively.

After 11 years developing geomorphology projects applied to environmental restoration for the Spanish Ministry of the Environment, she was an Assistant Professor with the University of León, Spain. She is currently an Associate Professor of Geology with the University of Oviedo, Asturias, Spain.

Prof. Fernández is a member of Institute of Science and Aerospatial Technologies of Asturias. Her research interests include soil geomorphology and planetary science using spectroscopy, remote sensing, and GIS techniques.

Alejandro Corbea-Pérez was born in La Habana, Cuba, in 1991. He received the B.S. degree in meteorology from the Higher Institute of Technology and Applied Science, La Habana, Cuba, in 2015, and the M.S. degree in remote sensing and geographical information systems from the University of Oviedo, Asturias, Spain, in 2017. He is currently working toward the Ph.D. degree in biogeosciences with the University of Oviedo, Asturias, Spain.

His research interest includes the study of temperature and albedo in Antarctica using satellite and weather station data.

Juanjo Peón received the B.S. degree in geomatics and topography engineering, the M.S. degree in remote sensing and geographical information systems, and the Ph.D. degree in biogeosciences from the University of Oviedo, Asturias, Spain, in 2011, 2013, and 2019, respectively.

He is currently a Postdoctoral Researcher with the Department of Mining Exploitation and Prospecting, University of Oviedo, working on optical remote sensing for planetary geology. His research interests include optical and thermal remote sensing, hyperspectral imaging and spectroscopy for a wide range of geoscience applications, such as the estimation of soil properties, surface temperature and albedo, and mapping of burned areas.

Jaime Otero received the M.S. degree in mathematics from Universidad Complutense de Madrid, Madrid, Spain, in 1998, and the Ph.D. degree in mathematics from Universidad Politécnica de Madrid, Madrid, Spain, in 2008.

He is currently an Associate Professor of Applied Mathematics with Universidad Politécnica de Madrid, Madrid, Spain, and a member of the Group of Numerical Simulation in Science and Engineering. His research interests include dynamics of marine-terminating glaciers and glaciological applications of geostatistics.

Francisco Navarro received the M.Sc. degree in physical sciences (geophysics) from Universidad Complutense de Madrid, Madrid, Spain, in 1983, and the Ph.D. degree in physical sciences from Universidad Politécnica de Madrid (UPM), Madrid, Spain, in 1991.

He was a Research Associate with the University of California Los Angeles, Los Angeles, CA, USA. He is currently a Professor of applied mathematics with UPM, leading its Group of Numerical Simulation in Science and Engineering. His research focuses on glacier dynamics.

Prof. Navarro is currently a President of the International Glaciological Society.